JOURNAL OF MATERIALS SCIENCE **32** (1997) 863–872

Microstructural characterization of high velocity oxy-fuel sprayed coatings of Inconel 625

H. EDRIS, D. G. McCARTNEY
Department of Materials Engineering and Materials Design, University of Nottingham, University Park, Nottingham NG7 2RD UK

A. J. STURGEON
TWI, Abington Hall, Abington, Cambridge CB1 6AL UK

High velocity oxy-fuel (HVOF) thermal spraying is being increasingly used to deposit high quality surface coatings. In the present study HVOF spraying was used to deposit coatings of the Ni-based alloy Inconel 625 onto mild steel substrates and the structure of the sprayed coatings were related to the processing conditions employed. The microstructural characteristics of the deposits were investigated using X-ray diffraction together with optical, scanning electron and transmission electron microscopy. The as-sprayed microstructure was found to consist of Ni-based metallic regions together with oxides exhibiting the Cr_2O_3 and $NiCr_2O_4$ crystal structures. Transmission electron microscopy revealed that although the metallic regions were predominantly highly alloyed, Ni-rich grains (depleted in solute) were also present in all coatings. Three processing variables were examined: oxygen to fuel gas ratio, total gas flow rate in the gun and combustion chamber length. All were found to significantly influence the oxide contents of coatings as measured by X-ray diffraction methods.

1. Introduction

In recent years there has been a growing interest in the use of high velocity oxy-fuel (HVOF) thermal spraying for depositing protective coatings of various materials on a wide variety of substrates [1]. In the HVOF process oxygen and a fuel (commonly a gas) are mixed and burnt in the combustion chamber of a spray gun. High gas temperatures and velocities are obtained and are used to heat and accelerate powder particles injected into the gun by a carrier gas stream [2]. Flame temperatures of typically around 2800 °C and gas velocities of up to $1600\,\mathrm{m\,s^{-1}}$ have been reported [3, 4]. The injected powder particles are rapidly heated and accelerated towards the substrate by the combustion, achieving velocities of the order of $450\,\mathrm{m\,s^{-1}}$ [5] before impact. The powder particle temperatures are believed to be relatively low and particle velocities high in comparison with other thermal spraying processes such as air or vacuum plasma spraying [4]. It is thus possible to minimize powder reaction with, or decomposition in, the gas stream by careful control of processing parameters. Consequently HVOF spraying can produce high quality, low porosity coatings which are well bonded to the substrate.

It is in the field of wear-resistant cermet-type coatings that HVOF has been most widely applied. For example, much work has been done on optimizing the processing parameters to achieve high specification WC–Co or Cr_3C_2–NiCr coatings for commercial applications [6–10]. The possibilities of applying the HVOF process to a much wider range of materials are now being addressed and there are several reports in the literature relating to the spraying of Ni and other metallic alloys for corrosion resistant applications where dense, microstructurally homogeneous coatings are essential [11–14]. Specifically, Harvey *et al.* [14] have, in a recent paper, highlighted the importance of reducing the bulk oxygen content of the as-sprayed Ni–Cr based alloy Inconel 625 in order to obtain a corrosion resistance approaching that of the wrought alloy.

The purpose of the present work was to undertake a detailed microstructural examination of selected coatings from the previous study [14], and to correlate changes in selected processing parameters with microstructure formation.

2. Experimental procedure

2.1. HVOF spraying

A commercial, gas atomized Inconel 625 powder (Plasmalloy AI 1625 TG) was utilized for the study. The nominal composition of the alloy was Ni–22% Cr–9% Mo–4% Nb–2% Fe–0.4% Si–0.3% Mn (in wt %) with a nominal powder size distribution of $-66+22\,\mu\mathrm{m}$. The oxygen content of the powder was determined to be 340 p.p.m. by weight. The powder was sprayed onto low carbon steel substrates to a thickness of approximately 250 μm using a UTP/Miller Thermal

0022–2461 © *1997 Chapman & Hall*

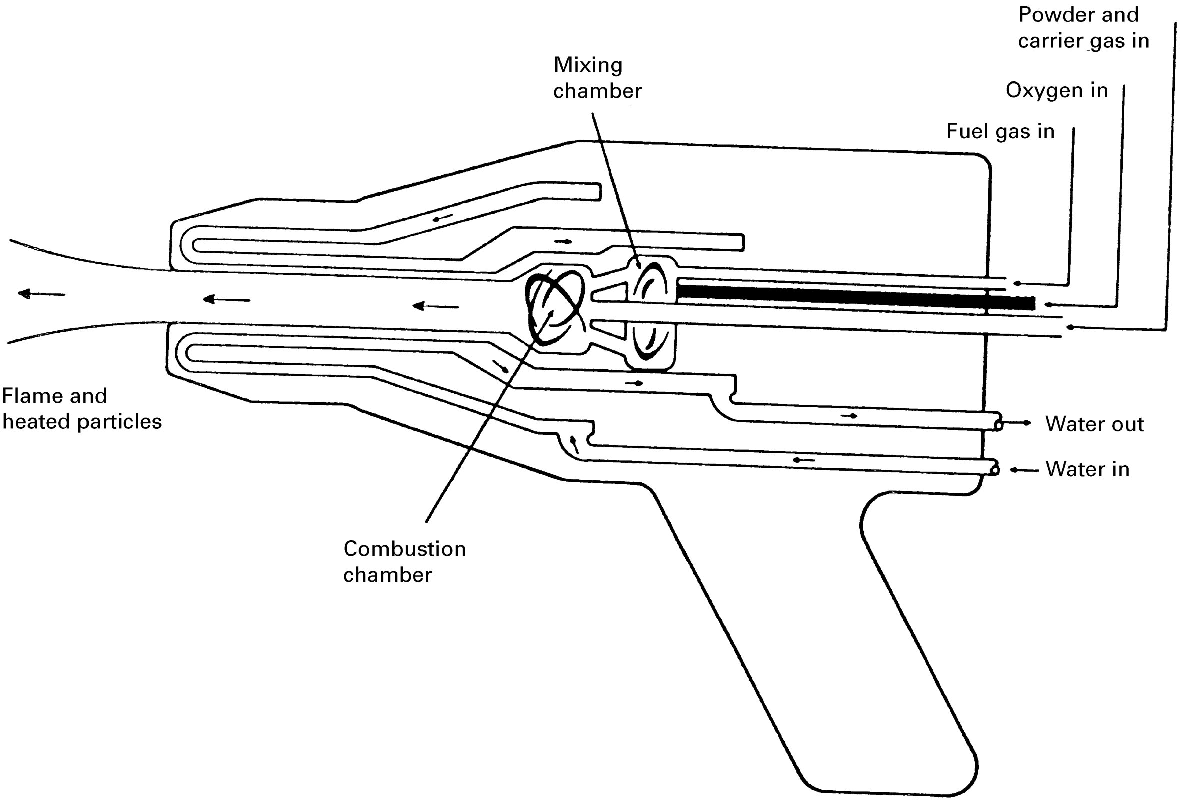

Figure 1 Schematic illustration of a UTP Top Gun for high velocity oxy-fuel spraying.

high velocity oxy-fuel (HVOF) system. The design of the spray gun is shown schematically in Fig. 1. Gas flow rates to the gun were set using a volume control system for fuel gas, oxygen and carrier gas. Powder was fed to the gun using an argon carrier gas and in this study propylene, C_3H_6, was employed as the fuel gas. For each set of spraying conditions a number of mild steel substrates were mounted onto a turntable with a vertical axis of rotation which was placed in front of the gun at the required stand-off distance. The traverse rate of the substrate across the spray was controlled by the rotation rate of the turntable. The gun was aligned perpendicular to the turntable axis of rotation and moved up and down the axis at a speed of 2.5 mm s^{-1}. In this way flat substrates typically 25 mm by 50 mm by 5 mm thick were coated.

There are a large number of processing variables in HVOF spraying, and the present samples formed a sub-set of the previously described [14] matrix of experiments, designed to identify the influence of process variables on corrosion resistance of the coatings.

TABLE I Manufacturer's recommended spray parameter settings

Parameter	Setting
Chamber size (mm)	0
Stand off distance (mm)	254
Traverse rate (m s^{-1})	0.93
Total gas flow (l min^{-1})	337
Oxygen to fuel gas ratio	3.4
Carrier gas flow (l min^{-1})	14
Powder feed rate (g min^{-1})	45

TABLE II Parameter settings for the samples examined

Sample	P1	P2	P3	P4	P5	P6	P7
Combustion chamber size (mm)	0	0	0	0	12	12	12
Total gas flow rate (l min^{-1})	286	337	203	286	286	337	286
Oxygen to fuel gas ratio	3.4	4.1	4.1	3.0	3.0	3.0	4.1

The gun manufacturer's recommended operating parameters for spraying Inconel 625 are listed in Table I. All parameters were held constant except the combustion chamber size, oxygen gas to fuel gas ratio and total gas flow rate as these three were found to have the most significant effect on corrosion performance. For the work described in this paper seven samples were subjected to detailed microstructural investigation and the values of the above parameters for each of the samples are given in Table II.

2.2. Characterization

Powder particle morphologies were studied in a scanning electron microscope (SEM) by sprinkling a small quantity of the powder onto an adhesive stub and imaging using the secondary electron signal. The powder particle size distribution was determined from semi-automatic image analysis of secondary electron micrographs. Cross-sections of the powder particles were prepared by mounting the particles in resin and then grinding and polishing. These were imaged in the SEM using the backscattered electron (BSE) signal.

Coating samples were examined by optical and scanning electron microscopy (SEM) as well as by X-ray diffraction (XRD). For optical microscopy and SEM, samples were cut from coating transverse sections, mounted in resin and then prepared by standard metallographic procedures. Prior to optical microscopy they were electroetched in 10% oxalic acid at 2 V. SEM samples were viewed in the as-polished condition using either secondary electron or BSE signals to form the image. Composition analysis was performed in the SEM using a Noran energy dispersive X-ray analysis (EDXA) system, with a thin-window detector capable of analysing elements down to carbon. A correction procedure known as the $\phi(\rho z)$ method [15] was used to obtain quantitative results.

In order to determine the crystallography and lattice parameters of phases present in powders and coatings they were subjected to XRD analysis using a Siemens Daco diffractometer operated at 40 kV with monochromatic CuK$_\alpha$ radiation and a scanning rate of 1.5 degrees/min. Furthermore, software based on the Chung method [16–18], and calibrated for intensity ratios using high purity Ni, Inconel 625 and Cr_2O_3 powders, was used to determine the relative amounts of metallic and oxide phases present in coatings sprayed under different conditions.

Samples of coatings for transmission electron microscopy (TEM) were cut from sections taken parallel to the coating surface and approximately midway between the surface and the coating – substrate interface. After initial grinding, twin-jet electropolishing was undertaken using 10 vol % perchloric acid in acetic acid at 10 °C and 12 V. TEM was conducted at 200 kV on a Jeol 2000 FXII also fitted with a Noran EDXA system.

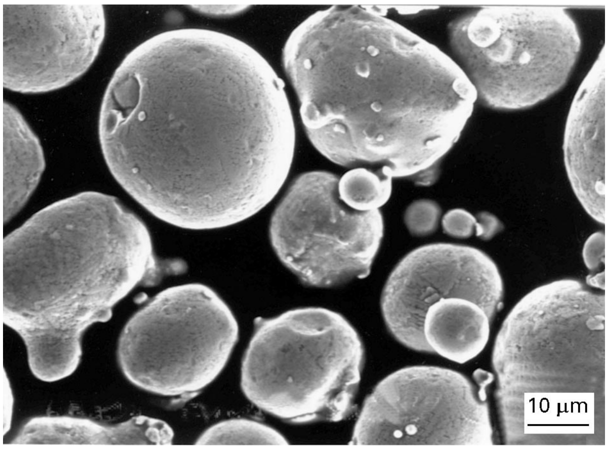

Figure 2 Secondary electron image of Inconel 625 powder particles showing a near spherical shape with a range of particle sizes. A dendritic substructure is visible on the surface of larger particles.

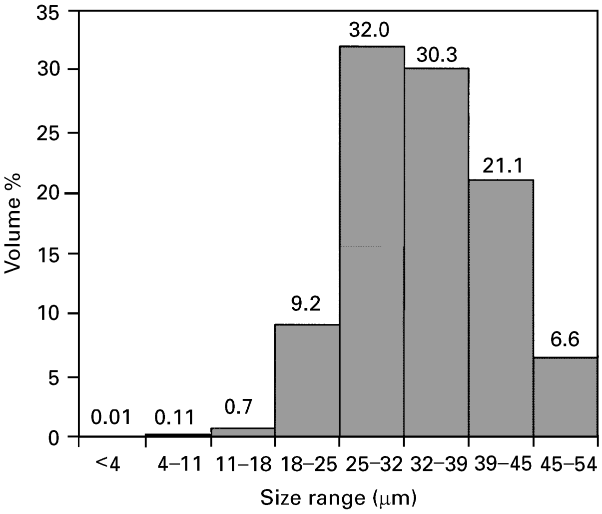

Figure 3 Powder particle size distribution histogram as determined by image analysis. The numbers by each column indicate the volume percentage in the size range.

3. Results

3.1. Inconel 625 powder

The as-received powder was examined both by X-ray diffraction and scanning electron microscopy. From the XRD pattern it was deduced that the powder was single phase, or at least the volume fractions of any secondary phases were below the limit of detection. The powder exhibited face centred cubic (f.c.c.) crystallography with a lattice parameter of 0.3597 nm as obtained by linear regression against $\cos^2\theta/\sin\theta$ with a correlation coefficient of 0.96. This is significantly larger than the lattice parameter of pure Ni which is 0.3524 nm [19].

Examination in the SEM confirmed that the powder had been produced by inert gas atomization in that the majority of the particles were near-spherical although a number had small satellites attached. These features can be seen in the secondary electron image shown in Fig. 2. The particle size ranged typically from 15–45 μm and a dendritic substructure is visible on the external surface. The satellite particles were typically 5–10 μm in size. The microsegregation, resulting from rapid solidification, was revealed by polishing the powder and examining particle cross-sections using back scattered electron imaging. A secondary dendrite arm spacing of about 1–2 μm was noted which is consistent with the gas atomization production route. EDXA was used to determine average powder particle compositions by examining small areas approximately 10 × 10 μm. The average composition, by this technique, was found to be 22.8 wt % Cr, 9.5 wt % Mo, 4.5 wt % Nb, 1.8 wt % Fe, remainder Ni, which is in reasonable agreement with the nominal chemical composition for major alloying elements.

The powder particle size distribution, determined by image analysis of secondary electron micrographs such as that in Fig. 2, is plotted in the histogram of Fig. 3. There were no particles greater than 54 μm in diameter but it is clear that a significant powder fraction was less than 25 μm in size.

3.2. Inconel 625 coatings

3.2.1. X-ray diffraction analysis

X-ray diffractometer (XRD) scans from all the coatings gave peaks which could be identified as belonging

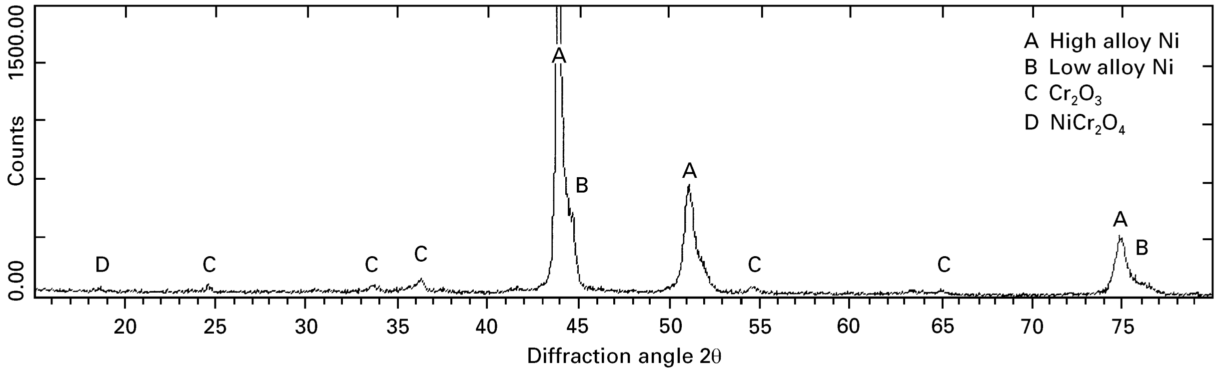

Figure 4 XRD scan in the range $2\theta = 15$ to 18° for coating sample P6 showing peaks belonging to Cr_2O_3 (C), $NiCr_2O_4$ (D) and a f.c.c. phase of lattice parameter 0.3590 nm. Small secondary peaks close to the main f.c.c. phase peaks are just apparent. A, high alloy Ni; B, low alloy Ni.

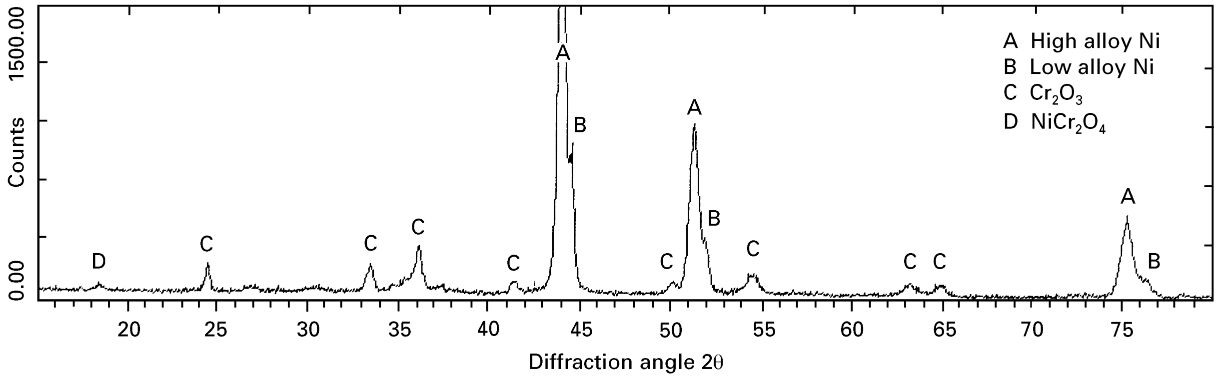

Figure 5 XRD scan for coating sample P2 showing more prominent secondary peaks close to the main f.c.c. phase peaks. Cr_2O_3 (C) and $NiCr_2O_4$ (D) phase peaks are also present. A, high alloy Ni; B, low alloy Ni.

to the following: Cr_2O_3, $NiCr_2O_4$ and a f.c.c. phase with a lattice parameter of approximately 0.3590 nm. A typical XRD scan, from coating P6, is shown in Fig. 4. The $NiCr_2O_4$ peaks were of low intensity in all coatings with only those at $2\theta = 18.5$ and 30.5° being detectable. It is clear that in the case of coating P6 the f.c.c. phase must be based on highly alloyed Ni since its lattice parameter is close to that of the gas atomized Inconel 625 powder. However, careful examination of XRD scans from P6 and other coatings revealed a series of secondary peaks at 2θ values close to those of the main peaks from the highly alloyed Ni. An example of prominent secondary peaks is shown in Fig. 5 which is an XRD scan taken from sample P2. The secondary peaks were noted to be much less prominent in the data from coatings P5 and P6 than from P1, P2 and P3. An analysis of the secondary peak positions showed that they occur at 2θ values corresponding to a f.c.c. phase with a lattice parameter of approximately 0.3530 nm, i.e. very close to the lattice parameter value of pure nickel. Thus, these secondary peaks could well arise from the presence in the coatings of Ni-rich regions with low alloy content. It should be emphasized that these observations were extremely reproducible and similar data were obtained when XRD scans were performed on different regions of the same coatings.

From the X-ray data it was possible to calculate values of the lattice parameter of the highly alloyed Ni-phase in each coating using established methods of regression against either $\cos^2\theta$ or $\cos^2\theta/\sin\theta$ and the values are given in Table III. The somewhat low correlation coefficients in a number of the samples reflect the significant broadening of peaks obtained from coatings compared with those from the original gas atomized powder for which a correlation coefficient of 0.96 was obtained. The clear trend apparent from Table III is that in coatings P5 and P6 the highly alloyed Ni-phase had significantly larger lattice parameters than in the coatings P1, P2 and P3 with the coatings P4 and P7 falling between the two extremes.

TABLE III Values of the high alloy Ni-phase lattice parameter (a) in each of the coatings obtained by linear regression against either $\cos^2\theta$ (column 2) or $\cos^2\theta/\sin\theta$ (column 3)

Sample	Regression against $\cos^2\theta$		Regression against $\cos^2\theta/\sin\theta$	
	a (nm)	r^2	a (nm)	r^2
P1	0.3586	0.70	0.3579	0.62
P2	0.3580	0.38	0.3576	0.31
P3	0.3576	0.80	0.3572	0.66
P4	0.3590	0.85	0.3583	0.82
P5	0.3597	0.79	0.3596	0.95
P6	0.3598	0.93	0.3594	0.95
P7	0.3589	0.87	0.3583	0.91

r^2 = correlation coefficient.

TABLE IV Intensity ratios I_1 and I_2 in different coating samples

Sample	I_1	I_2
P1	0.11	0.34
P2	0.13	0.40
P3	0.11	0.36
P4	0.07	0.22
P5	0.04	0.10
P6	0.05	0.18
P7	0.06	0.23

I_1 refers to the Cr_2O_3 line at $2\theta = 36.5°$ and I_2 to the low alloy Ni secondary peak at $2\theta = 44.5°$. The $\{1\,1\,1\}$ high alloy Ni-phase peak at $2\theta = 43.9°$ was used as the reference intensity in each case.

TABLE V Weight percentages of Cr_2O_3, high alloy and low alloy nickel regions present in the coating samples as determined from XRD analysis

Sample	P1	P2	P3	P4	P5	P6	P7
wt % high alloy Ni	73	68	73	79	87	81	81
wt % low alloy Ni	9	10	8	7	5	7	6
wt % Cr_2O_3	18	22	19	14	8	12	13

The diffractograms were also analysed in terms of intensity ratios of the high alloy Ni, low alloy Ni and Cr_2O_3 phases. The most intense Cr_2O_3 line at $2\theta = 36.5°$ and the strongest Ni secondary peak at $2\theta = 44.5°$ were ratioed to the $\{1\,1\,1\}$ high alloy Ni-phase peak at $2\theta = 43.9°$. Results are summarized in Table IV. Once again clear differences emerge between samples. The coatings P5 and P6 exhibit lower intensity ratios for both Cr_2O_3 and the low alloy Ni-phase secondary peaks than the coatings P1, P2 and P3. Furthermore the magnitude of the intensity ratio I_1 (for Cr_2O_3) correlates directly with that of I_2 (for low alloy Ni phase).

In addition to examining peak intensity ratios the weight percent of Cr_2O_3 in each coating was determined using the Chung method [16–18] and the values obtained are listed in Table V. Once again there is a clear trend with P5 and P6 having lowest Cr_2O_3 contents, P1, P2 and P3 the greatest oxide contents and the values for P4 and P7 intermediate between the two extremes. In this analysis the quantity of $NiCr_2O_4$ was too small to be reliably measured and so is neglected in the weight fraction calculations.

3.2.2. Optical microscopy, SEM and TEM

An optical micrograph of a typical region from a cross-section of coating P1 is shown in Fig. 6. Little porosity is visible in the coating which is seen to have a layered structure typical of thermally sprayed deposits. The light and dark regions are probably metallic and oxide phases respectively, and there was no evidence for a change in the proportions through the coating thickness. Optically, coatings from the range of samples were very similar with the P5 and P6 samples exhibiting less evidence of oxide stringers.

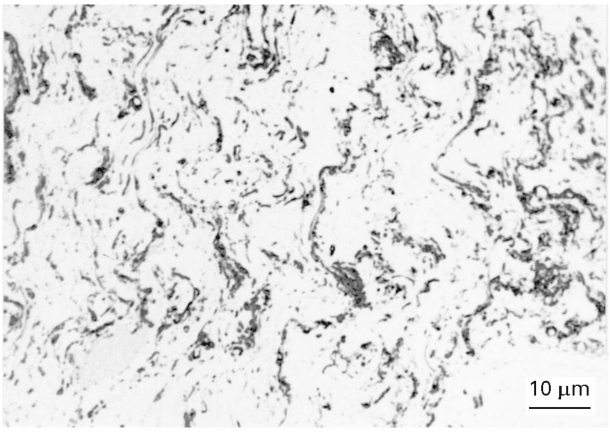

Figure 6 Optical micrograph of an etched transverse section of coating P1 showing a layered microstructure.

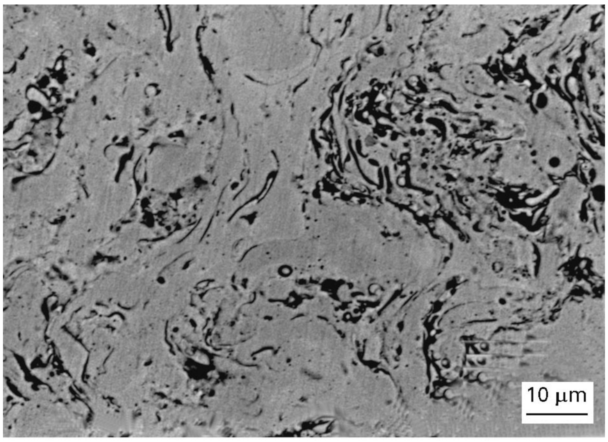

Figure 7 Backscattered electron image of a transverse section of coating P1 showing dark rounded areas which are pores, thin, dark-contrast stringers which are rich in oxygen and a lighter contrast metallic matrix.

More detailed information about the microstructure was obtained through EDXA on the SEM and a typical area of a coating cross-section is shown in Fig. 7 which was obtained using backscattered electrons to form the image. A number of regions of different contrast can be discerned. The darkest rounded features were identified as pores. The areas of lighter contrast and the thin dark stringers were analysed using EDXA, and spectra from typical light areas and grey stringers are shown in Fig. 8a and b, respectively, whilst average compositions of the regions of different contrast are listed in Table VI. Because the dark stringers were relatively thin their analysis values could, of course, include a contribution from the surrounding matrix. The light areas, which constituted the majority of the coating, are seen, from Table VI, to have a composition similar to that of the gas atomized Inconel 625 with no detectable oxygen. On the other hand the grey stringers contained significant amounts of oxygen and were enriched in Cr, Nb and Mo relative to the brighter matrix regions. The stringers of Fig. 7 are therefore almost certainly the Cr_2O_3 and $NiCr_2O_4$-based phases identified by XRD whereas the lighter matrix areas are metallic. A small number of unmelted particles could also be identified

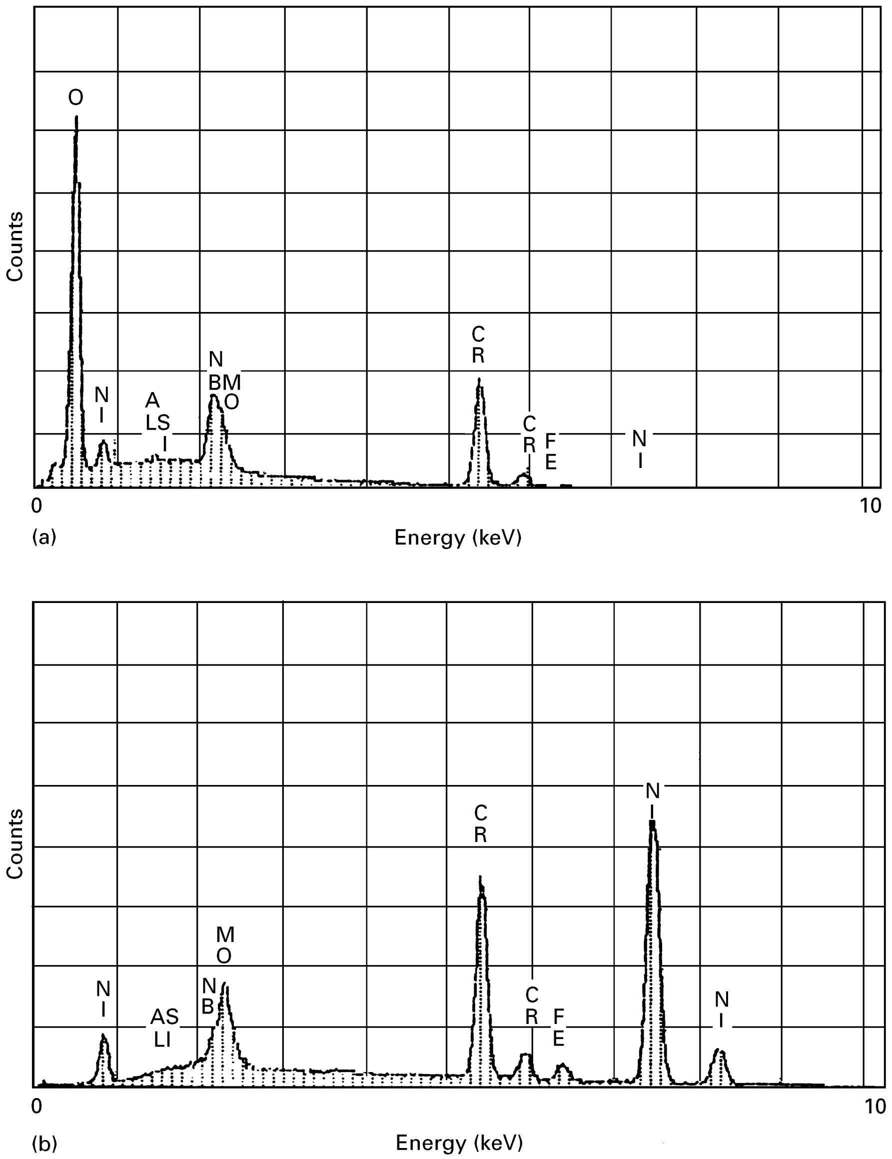

Figure 8 EDXA spectra obtained in the SEM from the thin dark stringers (a) and light contrast matrix regions (b) of Fig. 7. The spectra show that the stringers were rich in O, Cr, Nb and Mo whilst the matrix contained principally Ni, Cr, Mo, Nb and Fe.

TABLE VI Average compositions (wt %) of the phases present in coatings as determined by EDXA in the SEM

	Element (wt %)				
Phase	Cr	Mo + Nb	Fe	O	Ni
Oxides	40 ± 5	17 ± 4	1.5 ± 0.5	34 ± 3	4 ± 2
Alloy	20 ± 2	14 ± 1	2.3 ± 0.3	–	63 ± 3

Oxide analyses contained significant contributions from the surrounding matrix.

by backscattered electron imaging and these were characterized by having a segregation pattern similar to that seen in gas atomized powders. However, their overall volume fraction in all the coatings examined was less than approximately 1%. In the SEM it was not possible to distinguish between high and low alloyed metallic regions which might have corresponded to the distinct peaks observed in the XRD spectra of Figs 4 and 5.

TEM of coatings was undertaken to obtain more detailed information on the nature of the oxide phases present and also to seek confirmation for the existence of metallic alloy phases with high and low alloy contents as suggested by the XRD data. Fig. 9a shows a bright-field TEM image of a region of a typical coating which exhibits a polycrystalline grain structure. The grains appear to be single phase with a grain size of the order of 200–500 nm. A selected area diffraction pattern from a large metallic grain of Fig. 9a is shown in Fig. 9b. The strong diffraction spots can be indexed according to a f.c.c. $\langle 1\,1\,0 \rangle$ zone axis pattern with a lattice parameter of approximately 0.359 nm i.e. close to the value obtained by XRD from the highly alloyed nickel phase. Furthermore, the EDXA spectrum of Fig. 9c shows the presence of the elements Ni, Cr, Mo, Nb and Fe but little oxygen was detected thus confirming that these large grains were highly alloyed metallic regions. Regions of much finer grain size were also present as shown in Fig. 10a together with the associated ring diffraction pattern and EDXA

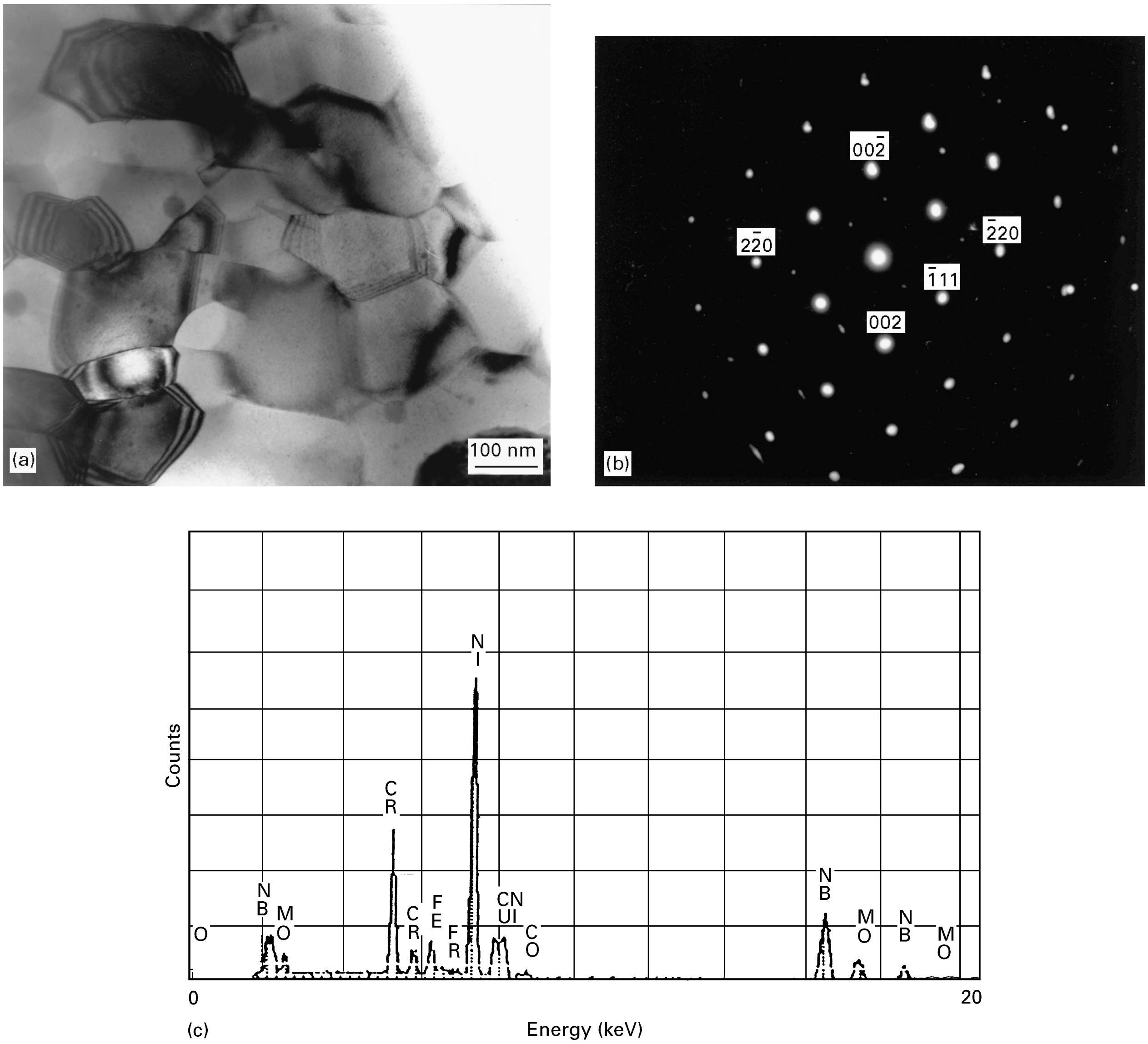

Figure 9 (a) Bright field TEM micrograph taken from a typical coating in which grains approximately 0.5 μm in size are visible. (b) Selected area diffraction pattern with the aperture centred over one of the large grains in (a). Strongest spots can be indexed as a ⟨1 1 0⟩ f.c.c. zone axis. (c) EDXA spectrum obtained from the centre of the grain which gave the diffraction pattern in (b) showing peaks due to Ni, Cr, Nb, Mo and Fe in this phase.

spectrum in Fig. 10b and c. From the EDXA analysis it is clear that a significant amount of oxygen was present in this phase as well as Cr, Ni, Nb and Mo. Clearly, though, the Ni content was significantly less than that of the metallic grains of Fig. 9. The ring diffraction pattern can be indexed according to the diffraction data given for the $NiCr_2O_4$ spinel phase [19] and hence it would seem that the crystal structure is based on the spinel but with the elements Mo and Nb substituting for some Ni and/or Cr. Grains which were chromium- and oxygen-rich (with only small amounts of Mo and Nb), and 100–500 nm in size, could also be seen in the TEM and these were found to have the crystallography of Cr_2O_3, thus confirming the XRD identification of this phase.

Finally, in coatings with a high oxide content (as measured by XRD) such as P1, P2 and P3 it was also possible to detect, in TEM samples, metallic grains which were Ni rich and of low alloy content. These imaged in a similar way to those shown in Fig. 9, but were of distinctly different chemical composition as shown by the typical EDXA spectrum of Fig. 11. This spectrum illustrates clearly that only small amounts of Cr, Nb and Mo were present in a Ni-rich matrix.

4. Discussion

The microstructures of these Inconel 625 coatings, as revealed by optical and scanning electron microscopy, exhibit a characteristic, lenticular, layered appearance. Metallic layers are seen to be typically 5–10 μm thick and are separated by what are apparently oxide sheets around 1–2 μm thick. This type of structure is similar to that previously reported for HVOF sprayed metallic alloys [11, 14, 20] and is consistent with a deposition process in which build-up occurs by oxide-coated liquid droplets impacting on the substrate, spreading, flattening and solidifying.

The XRD analyses combined with TEM have shown that the phases which formed were independent of the precise spray conditions in the range investigated, but their relative amounts varied significantly

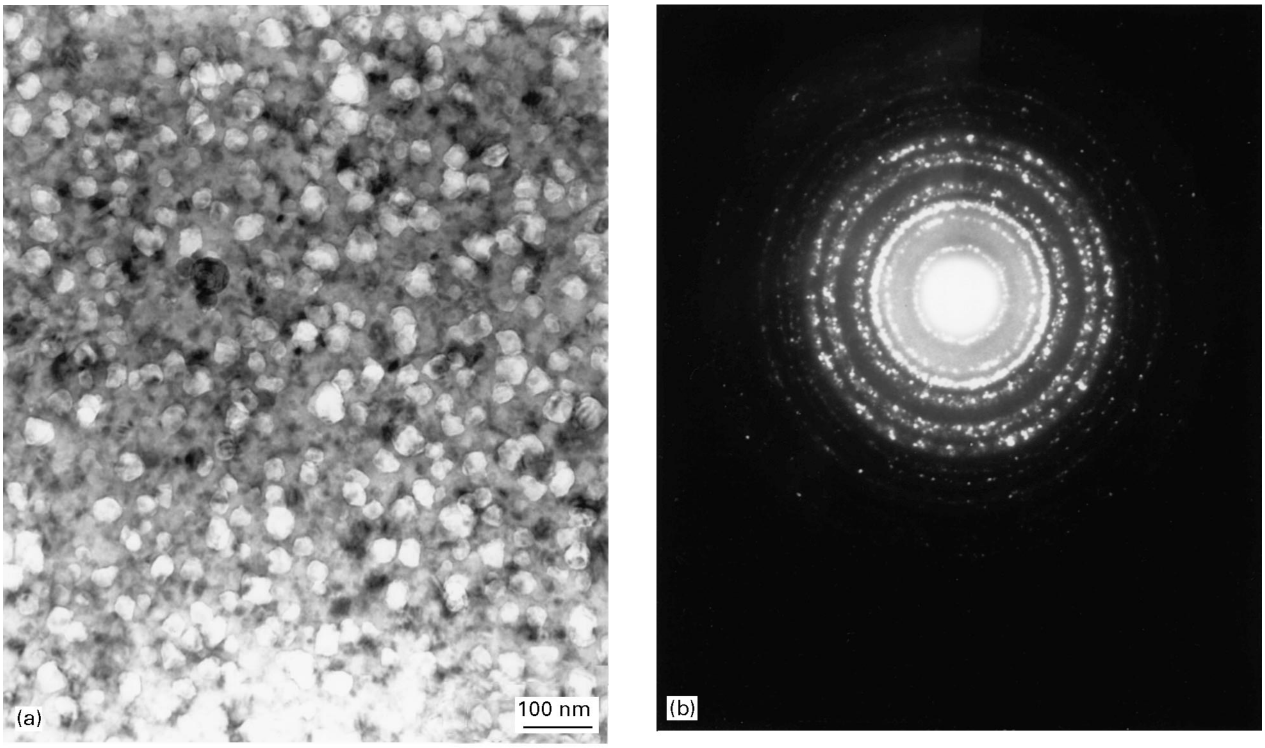

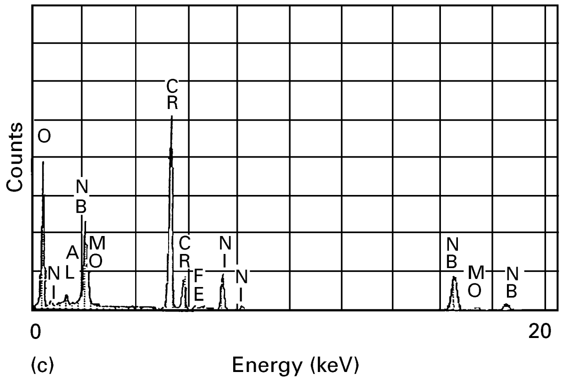

Figure 10 (a) Bright field TEM micrograph showing a fine grained region present in a typical coating. (b) Ring diffraction pattern taken from the polycrystalline region shown in (a). The rings can be indexed according to the $NiCr_2O_4$ crystal lattice. (c) EDXA spectrum from the fine grained region of (a) showing a prominent oxygen peak together with those from Ni, Cr, Mo, Nb.

with the three process parameters varied in this study. Each coating had a complex structure comprising a high alloy Ni-based phase, a low alloy Ni-based phase and oxide phases with the crystal structures of Cr_2O_3 and $NiCr_2O_4$ (spinel). Previous studies of HVOF sprayed Ni-based coatings have generally not examined the microstructure formation in such detail, although NiO and not Cr_2O_3 was reported to form in a Ni–20 wt % Cr binary alloy deposited with a different type of HVOF gun [11]. It is important to note that although EDXA on the SEM can be used to distinguish between oxide and metallic phases, this technique alone was unable to reveal the full details of the microstructure. Only through a combination of XRD and TEM of thin foils could the existence of distinct low and high alloy metallic regions and two types of oxide be confirmed.

Considering firstly the metallic phases, it is clear from XRD that high alloy f.c.c.-Ni was the major metallic phase but there was an appreciable fraction of the lower alloy Ni in those coatings which had higher oxide contents, as the data in Table V reveals. TEM confirmed the presence of both highly alloyed Ni as well as low alloy Ni and showed that both types of

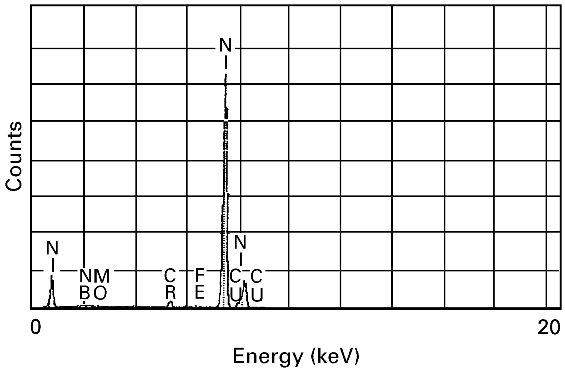

Figure 11 EDXA spectrum, obtained in the TEM, from a region of a coating with 100–200 nm sized low alloy metallic grains. Ni is the most prominent peak with only traces of Fe, Mo, Nb and Cr.

metallic regions had grain sizes typically less than 0.5 μm with no evidence of solidification segregation of solute. This indicates a rapid solidification rate within the impacting droplets; higher than that in the original gas atomized powder. With regard to the structure and composition of the oxide phases it is clear that the principal oxide phase was that with the Cr_2O_3 structure, as evidenced by the intensity of the XRD peaks. The spinel peaks were of such low intensity as to indicate that coatings always contained less than about 2 wt % of this phase. In the TEM the spinel was found to have a grain size ca. 50 nm whereas Cr_2O_3 grains were in the size range 200–500 nm. Furthermore, the spinel structure contained appreciable quantities of Nb and Mo along with Cr and Ni,

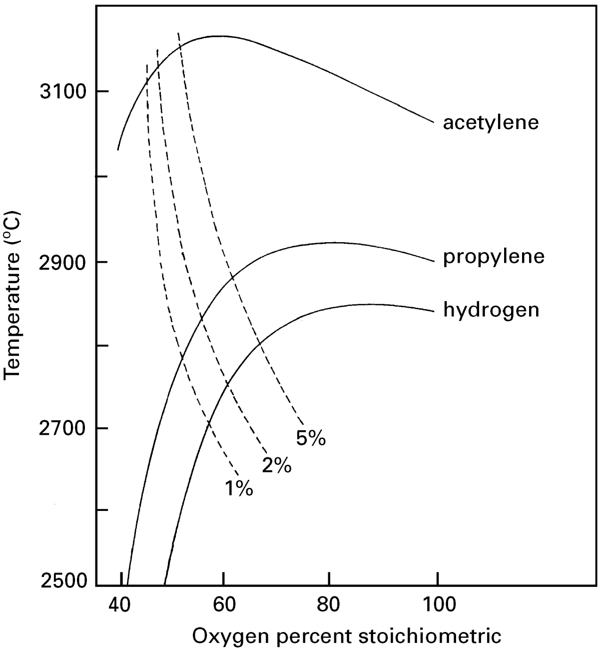

Figure 12 Graph of calculated flame temperature versus oxygen addition expressed as a percentage of that required for stoichiometric combustion for the gases acetylene, propylene, and hydrogen. Calculated excess oxygen in the flame is also shown by the dotted lines (taken from reference 3).

as Fig. 10c indicates, whereas the Cr_2O_3 contained smaller amounts of the elements Nb, Mo.

The formation of oxide phases is to be expected in HVOF spraying because of the nature of the high temperature gaseous environment both during combustion and in the free jet exhaust gas stream emerging from the nozzle. Hewitt [3] has calculated flame temperatures and excess oxygen in the flame for a range of gases and fuel to oxygen gas ratios. Fig. 12, which is taken from his analysis, shows the calculated variation of flame temperature with oxygen as a percentage of the stoichiometric requirement and also includes lines showing the calculated excess oxygen in the flame. The stoichiometric reaction for propylene is $C_3H_6 + 4.5O_2 \rightarrow 3CO_2 + 3H_2O$ giving an $O_2{:}C_3H_6$ stoichiometric ratio of 4.5. From this it is clear that even over the sub-stoichiometric range of gas ratios employed (67% to 91% stoichiometric) there would still have been excess oxygen available to drive oxidation of the metallic powder particles. In addition air would have been turbulently mixed into the exhaust gas jet as it left the gun. Although the precise temperature–time histories of individual particles cannot be easily determined, calculations show that most particles would have been expected to be molten for at least several milliseconds before hitting the substrate [4, 21]. The preferential formation of oxides of chromium is thus to be expected on thermodynamic grounds. According to Ellingham diagram data on standard free energies of formation of oxides [22], the thermodynamic stability of oxides will increase in the order Ni, Mo, Nb, Cr. Furthermore, it is well known [23] that solid Ni–Cr based alloys form the spinel $NiCr_2O_4$, as well as Cr_2O_3, on exposure to an oxidizing environment with the spinel being thermodynamically favoured at higher oxygen partial pressures. However, both Cr_2O_3 and the spinel have been reported to form in initial, transient oxidation [23] and so the underlying reasons for the formation of both types of oxide during spraying are, at least qualitatively, clear.

Turning now to the effect of process parameters on phase content and microstructure, Tables II and V summarize the relevant experimental data. Comparing, firstly, the Cr_2O_3 contents for samples P5 and P6 it is apparent that, over the range considered, the total gas flow rate had a measureable effect; an increase of about 20% in the flow rate significantly increased the oxide content of the coating. A comparison of samples P2 and P3 confirmed this. The oxygen to fuel gas ratio is also seen to be important in determining the oxide content as evidenced in the data for samples P5 and P7 or P4 and P1. The oxide content is seen to increase markedly with an increase in the oxygen to fuel gas ratio from 3.0 to 3.4 i.e. from 67 to 76% of stoichiometry. Finally it can be discerned from the samples P4 and P5 that the 12 mm combustion chamber size gave a significantly lower oxide content than the manufacturer's recommended size of 0 mm. Thus it is clear that the interaction between process parameters and microstructure formation are complicated in this particular spray system. However, it is reasonable to expect that the oxide content would increase with both the percentage excess oxygen in the flame and the total power input to the gun. The former is directly related to the oxygen:propylene ratio (as shown in Fig. 12) whilst the latter is dependent on the gas flow rate. The role of the combustion chamber size requires further investigation through modelling of the flow and combustion processes taking place.

Also of interest is the mechanism of formation of the low alloy and high alloy Ni-based metallic regions in all the coatings; a feature particularly prominent in the coatings of higher oxide content. A possible explanation could be the different thermal histories experienced by particles of different sizes. When particles are injected into a flowing gas stream they experience momentum and heat transfer. Mathematical models [4, 21] indicate that small particles follow the gas temperature and velocity more closely than do larger ones and therefore reach significantly higher temperatures. The flame temperature is around 2800 °C (depending on the gas ratio) and the evidence is that the majority of particles become hot enough to melt (melting point of Inconel 625 is approximately 1290 °C). If it is assumed that molten particles form an oxide skin around them, then the oxidation of Cr and other elements from the liquid will proceed relatively slowly providing the oxide remains intact. Should, however, the oxide layer rupture or become molten then oxidation would proceed much more rapidly. The melting point of Cr_2O_3 is $\approx 2440\,^{\circ}C$ and so it is clear that only the smallest powder particles would approach this temperature. SEM analyses of the gas atomized Inconel powder does indeed show a significant number of sub-ten micron particles, and these could account for the formation of the low alloy Ni-rich regions in coatings. In general, the low alloy regions found in coatings are too small to identify in the SEM but are readily dectable in the TEM which would support the view that they originate from the smaller powder particles in the feedstock.

5. Conclusions

1. The as-sprayed microstructure of Inconel 625 coatings has been found to consist of high and low alloy Ni-based metallic regions together with oxides exhibiting the Cr_2O_3 and $NiCr_2O_4$ (spinel) crystal structures.

2. Although XRD analysis revealed that all coatings contained double peaks around the 2θ values expected for f.c.c. Ni, TEM was required to confirm that these corresponded to high and low alloy Ni-phase regions respectively. Both types of metallic regions had a grain size of ca. 200 nm and there was no evidence for solidification segregation within the grains. This indicates that rapid quenching from the melt had occurred.

3. TEM of coatings also showed that the spinel phase, $NiCr_2O_4$, consisted of grains of around 50 nm in size and that it contained significant amounts of Nb and Mo in addition to Ni and Cr. On the other hand the grains of Cr_2O_3 were generally larger than 100 nm and contained only small amounts of Mo and Nb.

4. The relative amounts of the different phases present in coatings depended significantly on the three processing variables examined in the present study: oxygen to fuel gas ratio, combustion chamber length and total gas flow rate.

References

1. D. W. PARKER and G. L. KUTNER, *Adv. Mater. Proc.* **4** (1991) 68.
2. H. KREYE, in Proceedings of the 12th International Conference on Thermal Spraying, London, June 1989, edited by I. A. Bucklow (Abington Publishers, 1989) p. 313.
3. A. D. HEWITT, *Welding and Metal Fabrication* November 1972, 382.
4. E. B. SMITH, G. D. POWER, T. J. BARBER and L. M. CHIAPPETTA, United Technologies Research Centre Report 91-8, East Hartford, CT, 1991.
5. A. REUSCH, H. VOGGENREITER, H. HUBER and W. MAYR, *Metallurgy* **49** (1995) 38.
6. T. P. SLAVIN and J. NERZ, in Proceedings of the 3rd National Thermal Spray Conference, Long Beach, CA, May 1990, edited by T. F. Bernecki (ASM International, Metals Park, OH, 1991) p. 159.
7. Y. WANG and P. KETTUNEN in Proceedings of the 13th International Thermal Spray Conference, Orlando, FL, June 1992, edited by C. C. Berndt (ASM International, Metals Park, OH, 1992) p. 575.
8. M. SASAKI, F. KAWAKAMI, C. KOMAKI and M. ISHIDA, *ibid.* p. 165.
9. J. NERZ, B. KUSHNER and A. ROTOLICO, *J. Thermal Spray Technol.* **1** (1992) 147.
10. W. J. JAROSINSKI, M. F. GRUNINGER and C. H. LONDRY in Proceedings of the 5th National Thermal Spray Conference, Anaheim, CA, June 1993, edited by C. C. Berndt and T. F. Bernecki (ASM International, Metals Park, OH, 1993) p. 153.
11. R. KNIGHT and R. W. SMITH, in Proceedings of the 3rd National Thermal Spray Conference, Orlando, FL, June 1992, edited by C. C. Berndt (ASM International, Metals Park, OH, 1992) p. 159.
12. P. E. ARVIDSSON, in Proceedings of the 4th National Thermal Spray Conference, Pittsburgh, PA, May 1991, edited by T. F. Bernecki (ASM International, Metals Park, OH, 1991) p. 295.
13. D. J. VARACELLE Jr, M. G. ORTIZ, C. S. MILLER, A. J. ROTOLICO, J. NERZ, T. J. STEEPER and W. L. RIGGS, in Proceedings of the 3rd National Thermal Spray Conference, Orlando, FL, June 1992, edited by C. C. Berndt (ASM International, Metals Park, OH, 1992) p. 181.
14. M. D. F. HARVEY, A. J. STURGEON, F. L. BLUNT and S. B. DUNKERTON, in Proceedings of the 14th International Thermal Spray Conference, Kobe, Japan, May 1995.
15. S. J. B. REED, in "Electron microprobe analysis", (Cambridge University Press, Cambridge, 1993) p. 223.
16. F. H. CHUNG, *J. Appl. Crystallogr.* **7** (1974) 519.
17. *Idem., Ibid.* **7** (1974) 526.
18. *Idem., J. Appl. Crystallogr.* **8** (1975) 17.
19. JCPDS, International Centre for Diffraction Data, 1993, PDF # 4-850.
20. L. PAWLOWSKI, in "The science and engineering of thermal spray coatings" (John Wiley & Sons, Chichester, 1995) p. 177.
21. M. L. THORPE and H. J. RICHTER, *J. Thermal Spray Technol.* **1** (1992) 161.
22. D. R. GASKELL, in "Introduction to metallurgical thermodynamics" (McGraw Hill, New York, 1973) p. 269.
23. N. BIRKS and G. H. MEIER, in "Introduction to high temperature oxidation of metals" (Edward Arnold, London, 1983) p. 107.

Received 24 June
and accepted 31 July 1996